RESEARCH REPORT

VTT-R-00579-25

SAFER-FN-CAMP: Assessment of alkali-silica reaction and aggressive aqueous attack in concrete 2025

Authors: Yushan GU

Confidentiality: VTT Public
Version: 21.01.2026

beyond the obvious

Report's title

VTT internal reports-SAFER-FN-CAMP: Assessment of alkali-silica reaction (ASR) and aggressive aqueous attack (AAA) in concrete 2025

Customer, contact person, address -	**Order reference** -
Project name SAFER-Finnish Nuclear Concrete Ageing Management Project	**Project number/Short name** SAFER-FN-CAMP
Author(s) Yushan GU	**Pages** 22/
Keywords Alkali-silica reaction; Aggressive aqueous attack; durability of concrete; modelling.	**Report identification code** VTT-R-00579-25

Summary

This report summarises the study conducted in the SAFER-FN-CAMP project in 2025.

The primary objective of WP2 in the FN-CAMP project is to assess the deterioration mechanisms induced by alkali-silica reaction (ASR) and aggressive aqueous attack (AAA) of concrete structures in nuclear power plants (NPPs). To achieve this goal, assessment tools to predict the ASR expansion of concrete and evaluate the deterioration of concrete exposed to an aggressive aqueous environment were developed within the project.

The first section examines the use of the ASR assessment tool to evaluate the effect of loading confinement on ASR expansion: uniaxial, biaxial, and triaxial loading conditions.

In the second part, the durability performance of cementitious materials exposed to groundwater and seawater is predicted, and their degradation degrees are compared and assessed.

Confidentiality	VTT Public

Otaniemi, 21.1.2026

Written by	**Reviewed by**
Yushan GU, Research scientist	Miguel Ferreira, Research team leader

VTT's contact address

Tekniikantie 21, FutureHub, Espoo, 02150, Finland

Distribution (customer and VTT)

{Customer, VTT and other distribution. In confidential reports the company, person and amount of copies must be named. Continue to next page when necessary.}

Approval

VTT TECHNICAL RESEARCH CENTRE OF FINLAND LTD

Date:	21 January 2026
Signature:	Laitinen Tarja 912468625 Digitally signed by Laitinen Tarja 912468625 Date: 2026.01.22 10:05:44 +02'00'
Name:	Tarja Laitinen
Title:	Vice President

Contents

1. Introduction

The SAFER-FN-CAMP project aims to evaluate the safety performance of Finnish nuclear power plants (NPPs) and the concrete structures of radioactive waste repositories. The outcomes address ageing-related aspects based on the needs of Finnish End Users.

This report summarises the study conducted in WP2 of the SAFER-FN-CAMP project for 2025. Using the assessment tool developed in 2023 [1], sensitivity analyses were conducted. In 2024, WP2 investigated the deterioration mechanism induced by alkali-silica reaction (ASR) and evaluated the impact of temperature and relative humidity (RH) on ASR expansion [2]. In addition, WP2 assessed the durability performance of cementitious materials exposed to Na_2SO_4/and NaOH solutions, representing one of the considered aggressive aqueous attack (AAA) conditions.

In the final project year (2025), WP2 continues its study by assessing the impact of loading confinement on ASR expansion under uniaxial, biaxial, and triaxial loading conditions. Furthermore, WP2 evaluates the deterioration mechanisms and durability performance of materials exposed to groundwater and seawater, and compares their performance.

2. WP2 Alkali-silica reaction (ASR) and aggressive aqueous attack (AAA) on structural performance

2.1 T2.1 ASR on structural performance

This task is to develop an assessment tool to evaluate the deterioration of concrete subject to ASR. A thermo-chemo-cracking model [3] is adopted to simulate the ASR expansion, with some parameters characterising the property of the material. The basic model was established in 2023, calculating the incremental volumetric ASR strain and replicating the expansion curves of concrete subject to ASR. The model couples the kinetics of chemical reactions and the mechanics of cracking that affect volume expansion and the degradation of mechanical properties. To be more specific, it considers the impact of tensile cracking, compressive stresses, temperature, and RH based on empirical equations. The model is applicable in scenarios where volumetric expansion data for samples is available, and further studies on the effects of temperature, relative humidity, and loading constraints are required. It can replicate sample expansion and predict how environmental factors influence expansion behaviour.

Work in 2024 focused on analysing the impact of temperature and RH on ASR expansion and exploring the capabilities and limitations of the model. It was found that temperature influences the expansion rates, i.e., a higher temperature leads to faster kinetics. An impact of temperature on final expansion was observed, i.e., a higher temperature leads to a higher final expansion. This was because the final expansion was calculated based on incremental deformation as a function of time, where faster incremental kinetics at higher temperatures were considered. However, this was not consistent with the literature, where a limited or negative impact of temperature on final expansion was reported. Thus, it was recommended to use normalised expansion instead of final expansion in the current model. The impact of RH on ASR expansion was also investigated, and a threshold for initiating ASR was found. According to the sensitivity analysis results, no expansion was observed at an RH of 50%, slight expansion started when the RH increased up to 70%, and significant expansion was observed when the RH was above 90%. The findings suggested that employing a low relative humidity (RH) can help reduce ASR expansion.

In the current project year, the focus is on investigating the impact of confining stress on ASR expansion under various loading conditions, namely uniaxial, biaxial, and triaxial states.

2.1.1 Literature review

The ASR volumetric imposed strain can be considered as constant whatever the stress state [4]. However, [5] reported that the volumetric strains vary with stress state, particularly in the triaxially stressed conditions. It means that confinement plays a significant role in mitigating ASR-indued expansion [4]. In a series of tests under varying loading conditions, [6] observed that when a concrete cube was restrained in one direction, the strain in the unrestrained directions increased by approximately 25% compared to stress-free expansion, and by about 65% when restrained in two directions. Under multi-axial loading, some studies reported negligible or no ASR-induced expansion in the restrained directions [7], with no evidence of expansion transfer to less confined directions [8], [9]. Conversely, other investigations [4], [10], [11], [12], [13], [14] demonstrated that reducing ASR-induced expansion in the confinement direction often results in a compensatory increase in expansion in the unrestrained directions. The discrepancies are generally attributed to factors such as specimen scale, casting direction, confinement ratio, and directional effects [15]. The latter interpretation, expansion transfer, is more widely supported. This phenomenon leads to anisotropic development of ASR-related damage, which becomes more pronounced as ASR progresses [16]. Such anisotropy in confined concrete can cause significant deformation due to increased expansion in other directions, influencing stress distribution, damage generation and propagation, as well as crack patterns and orientations. This underscores the importance of understanding the anisotropic behaviour of ASR-affected concrete. To address this, a method was developed to calculate appropriate weighting factors and distribute the computed volumetric ASR strain across the three principal stress directions [3]. Detailed explanations of this method, along with examples for uniaxial, biaxial, and triaxial loading scenarios, will be presented in the following sections.

2.1.2 Calculation of weight factors

The influence of confining stress on ASR expansion is typically addressed by distributing the volumetric ASR strain among the principal directions using weight factors [3]. In essence, materials tend to expand preferentially along directions that are less constrained. As illustrated in Figure 1, consider section 1, where **uniaxial loading** is applied along the *k*-direction. In this scenario, the strain in the two unconstrained directions is relatively larger and equal, while the constrained direction exhibits minimal expansion. For **biaxial loading** in section 2, where a stress of σ_u is applied along the *l*-direction (σ_l). σ_u is the upper compressive stress beyond which ASR expansion is inhibited, thus expansion along the *l*-direction is completely restricted, and the volumetric strain is redistributed between the remaining two directions.

The situation becomes more complex under **triaxial loading** as illustrated in section 3, where all three directions experience varying degrees of confinement. To address this, a systematic approach is used to compute weight factors that govern how the volumetric strain is apportioned among the three directions. These weight factors ensure that the strain distribution reflects the relative constraints imposed by the applied stresses. A summary of specific cases and their corresponding weight factors is provided in Table 1.

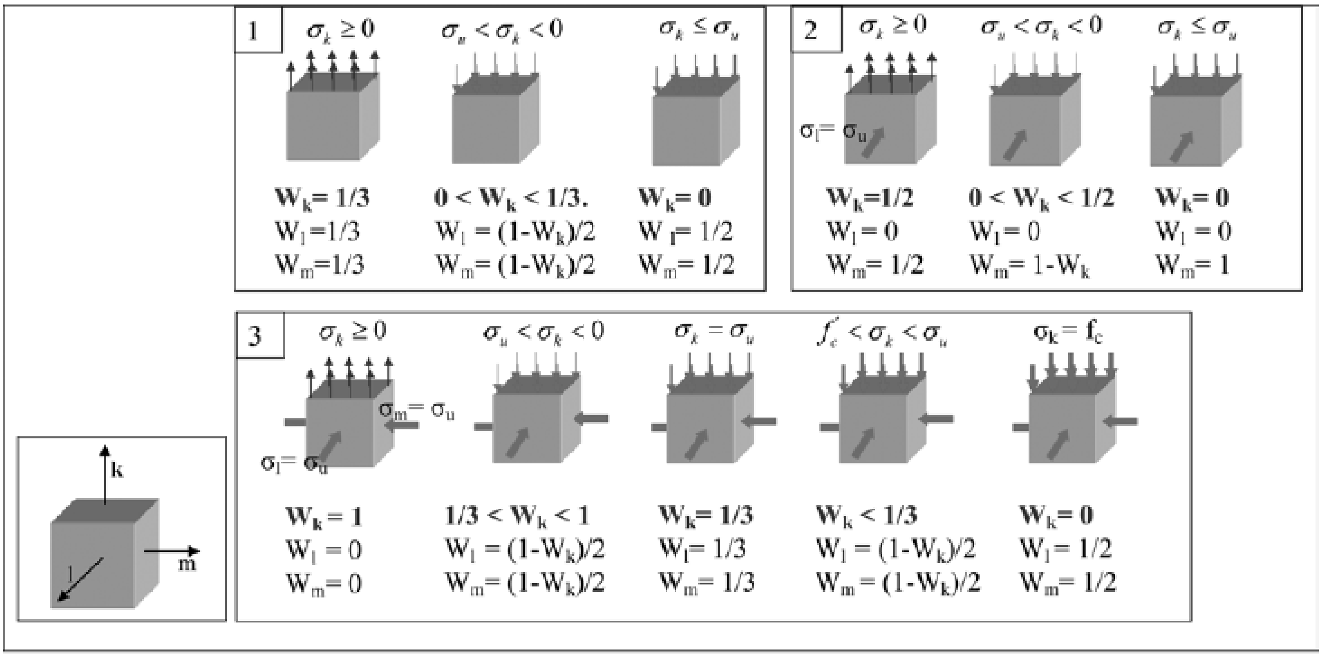

Figure 1: Weight of volumetric ASR redistribution in selected cases [3].

The method to calculate weight factors along three directions can be summarised into 4 Steps [3]:

Step 1: Identify the Quadrant

Refer to Figure 2, which illustrates the quadrant framework based on the stress state. The quadrant containing the stresses σ_l and σ_m must first be determined. In this framework:

- f_t represents the tensile strength,
- f_c denotes compressive strength, and
- σ_u is the upper compressive stress beyond which ASR expansion is inhibited along the corresponding direction.

Experimental studies have reported that ASR gel expansion ceases above certain compressive pressure limits. For instance, [17] observed no gel expansion beyond 11 MPa (compressive stress) using synthetic gel, while [3] and [18] confirmed a similar threshold at approximately -10 MPa. This behaviour is primarily attributed to external compressive loading, which inhibits ASR expansion and consequently limits gel formation. However, most studies focus on the stress-strain response, and quantitative characterisation remains scarce, likely due to the challenge of identifying gels.

Step 2: Determine Node Weights

Using Table 1, identify the weights of four neighbouring nodes within the selected quadrant. Apply linear interpolation based on the stress component σ_k to compute the preliminary weights W_i, where i corresponds to the four adjacent nodes.

Step 3: Compute shape factors

Calculate the shape factors N_i for each node within the quadrant using the following formulation:

$$N(\sigma_l \sigma_m) = \frac{1}{ab}\left[(a-\sigma_l)(b-\sigma_m)\sigma_l(b-\sigma_m)\sigma_l\sigma_m(a-\sigma_l)\sigma_m\right]$$

where: $a = (a_1|a_2|a_3)$, $b = (b_1|b_2|b_3)$

These shape factors represent the relative influence of each node within the quadrant.

Step 4: Calculate Final Weight Factor

Finally, compute the weight factor along the *k*-direction using the combined contributions of node weights and shape factors:

$$W_k = \sum_{i=1}^{4} W_i N_i$$

This aggregated weight factor ensures that the volumetric ASR strain is distributed proportionally among the three directions, reflecting the stress state and confinement conditions.

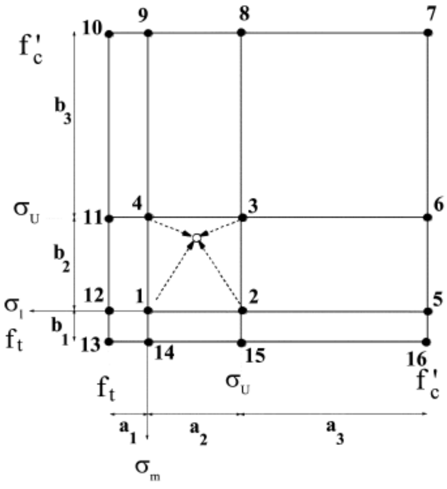

Figure 2: Weight regions [3].

			Weight direction k		
Point	σ_l	σ_m	$\sigma_k \geq 0$	$\sigma_k = \sigma_u$	$\sigma_k = f'_c$
1	0	0	1/3	0	0
2	σ_u	0	1/2	0	0
3	σ_u	σ_u	1	1/3	0
4	0	σ_u	1/2	0	0
5	f_c	0	1/2	0	0
6	f_c	σ_u	1	1/2	0
7	f_c	f_c	1	1	1/3
8	σ_u	f_c	1	1/2	0
9	0	f_c	1/2	0	0
10	f_t	f_c	1/2	0	0
11	f_t	σ_u	1/2	0	0
12	f_t	0	1/3	0	0
13	f_t	f_t	1/3	0	0
14	0	f_t	1/3	0	0
15	σ_u	f_t	1/2	0	0
16	f_c	f_t	1/2	0	0

Table 1: Weight factor in k-direction in triaxial loading cases [3].

Two representative examples from [19], involving two distinct loading conditions, were selected for analysis:

- **Case 1**: Stress state of [-9, -9, -1] MPa;
- **Case 2**: Stress state of [-9, -9, -9] MPa.

In this study [19], ASR expansion rates were measured along three principal directions, and the corresponding creep behaviour was subsequently derived. The measured proportions of expansion rates in each loading direction were then compared with the results calculated using the previously described method.

Using the calculation procedure described earlier, the weights of neighbouring nodes, shape factors, and weight factors were determined and are summarised in Table 2. Notably, the computed weight factors exhibit strong agreement with the experimental measurements reported in [19]. Specifically, the average weight factors from measurements were approximately (0.11, 0.07, 0.82) for **Case 1** and (0.33, 0.33, 0.33) for **Case 2**, confirming the consistency of the adopted methodology.

Table 2: Example of calculating weight factors in two cases.

Case	**1**	**2**
Loadings	[-9, -9, -1] MPa	[-9, -9, -9] MPa
Quadrant	1-2-3-4	1-2-3-4
$W_i(1,2,3,4)$	(0.3, 0.45, 0.933, 0.45)	(0.03, 0.05, 0.4, 0.05)
$N_i(1,2,3,4)$	(0.01, 0.09, 0.82, 0.09)	(0.01, 0.09, 0.82, 0.09)
(W_i, W_j, W_k) calculated from the method	(0.08, 0.08, 0.84)	(0.33, 0.33, 0.33)
Measured values [19]	(0.11, 0.07, 0.82)	(0.33, 0.33, 0.33)

The method is suitable for cases where the overall volumetric expansion rate of samples is known, but directional data is unavailable. It enables the determination of weighting factors for each direction, which are then used to estimate the expansion rate along individual directions. If we take **Case 1** as an example, with the volumetric expansion data and weighting factors for the three directions available, expansion curves for each direction can be easily plotted, as shown in Figure 3.

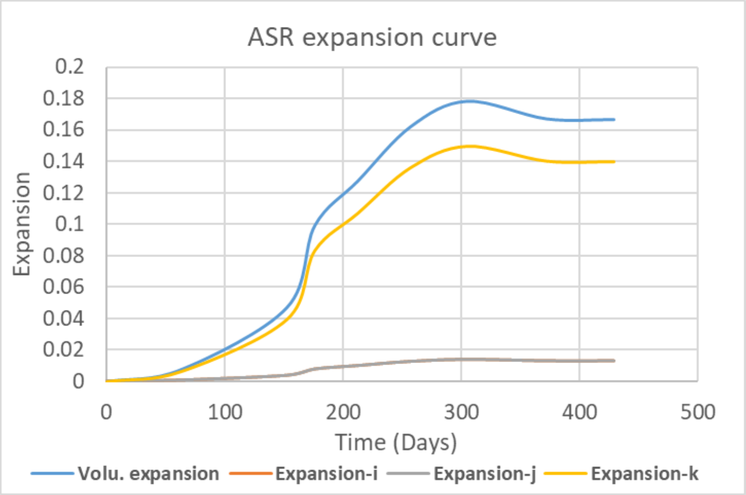

Figure 3: Expansion curves in volume and loading directions, with expansion in the i and j directions overlapping.

Among the limited studies addressing ASR behaviour under triaxial loading, [20] provides valuable insights. In this experimental work, the influence of creep and shrinkage was accounted for by subtracting the deformation measured on non-reactive specimens from that of reactive specimens, thereby isolating the net ASR-induced expansion. The findings confirm that triaxial stress constraints significantly reduce volumetric expansion and cause a redistribution of expansion from highly stressed directions toward less stressed ones.

For example, in Table 3, **Case 3**: under a uniform loading of [-3.9, -3.9, -3.9] MPa, the expansion was not perfectly isotropic; instead, a relatively higher strain was observed along the *i*-axis. Another case, **Case 4** with an imposed stress of [-9.6, -3.9, 0] MPa illustrates this directional effect more clearly: experimental results yielded weight factors of (0.134, 0.123, 0.744), whereas the predictive model estimated a distribution of (0.016, 0.301, 0.683). The expansion along the *i*-axis exhibited comparatively higher strain, despite the application of substantial compressive stress. The study did not provide an explanation for this observation. However, casting direction can influence ASR expansion, as anisotropic pore structure and aggregate orientation may cause directional variations in expansion behaviour.

Table 3: Example of calculating weight factors in two cases.

Case	**3**	**4**
Loadings	[-3.9, -3.9, -3.9] MPa	[-9.6, -3.9, 0] MPa
Quadrant	1-2-3-4	1-2-3-4
$W_i(1,2,3,4)$	(0.203, 0.305, 0.740, 0.305)	(0.03, 0.05, 0.4, 0.05)
$N_i(1,2,3,4)$	(0.372, 0.238, 0.152, 0.238)	(0.01, 0.09, 0.82, 0.09)
(W_i, W_j, W_k) calculated from the method	(0.333, 0.333, 0.333)	(0.016, 0.301, 0.683)
Measured values [19]	(0.446, 0.297, 0.257)	(0.134, 0.123, 0.744)

In addition to errors arising from experimental measurements, the discrepancies can be attributed to the fact that, as noted in [3], the model is largely based on the simplified assumptions presented in [18], [21], which do not account for creep and shrinkage and rely on “engineering common sense”. Nevertheless, the model successfully captures the primary expansion phenomenon, namely that materials tend to expand preferentially along less constrained directions. Furthermore, these assumptions make the model user-friendly and easy to apply.

The observed discrepancies, however, highlight the limitations of such generalised approaches and underscore the need for a more comprehensive predictive framework. Such a model should integrate chemical reaction kinetics, microstructural evolution of cementitious materials, and time-dependent phenomena such as creep and shrinkage to accurately capture ASR-induced expansion under complex stress states. It highlights the need to be considered in the next step.

To address this need, we are extending this study to a second phase (FN-CAMP II proposal submitted to SAFER 2028 call), proposing a multi-scale model to simulate ASR expansion. The goal of the proposal is to develop a robust numerical model capable of simulating the initiation and progression of concrete swelling induced by internal swelling reactions (ISR), including ASR and delayed ettringite formation (DEF). The model will incorporate key phenomena such as mineralogical alterations, crack formation, and crack intensity. To achieve this, the project aims to identify the degradation mechanisms associated with ASR and DEF through an extensive review of current literature at the nano- and micro-scales. Furthermore, the work will reproduce the chemical reactions driving ISR and the formation of expansive gels within cementitious materials, while also simulating the transport behaviour of moisture and reactive ions. A critical component of the study involves investigating cracking mechanisms and accurately modelling crack initiation and propagation. Beyond material-level analysis, the new project will explore the practical application of the developed assessment tool in real-world scenarios, such as NPP structures, and evaluate the feasibility of extending the approach to the structural scale, considering the influence of geometry and external loading conditions.

2.2 T2.2 AAA on structural performance

An assessment tool based on reactive-transport modelling is developed in this task to evaluate the deterioration of concrete exposed to an aggressive environment, which includes pure water, sodium sulfate solution, groundwater, and seawater. This order of solutions is determined according to the number of reactions that may occur between the material and the exposed solution.

In 2023, the performance of concrete exposed to leaching was simulated. The main degradation phenomenon observed was portlandite (CH) dissolution, calcium silicate hydrate (C-S-H) decalcification, and calcite precipitation. In 2024, the performance of concrete exposed to Na_2SO_4 solution was evaluated, and the profiles/evolution of the mineralogical phases and porosity were simulated. It was observed that cementitious phase changes starting from the replacement of monocarbonate by ettringite, followed by the dissolution of CH, decalcification of C-S-H, and precipitation of gypsum, in addition to ettringite. Gypsum was observed to dissolve when the pH decreased below 12.5. The durability of mortars was significantly improved when exposed to Na_2SO_4+NaOH solution, where a pH of 13 was maintained by adding NaOH to prevent leaching. Sensitivity analysis on the impact of the porosity of mortars was performed, and a longer service life was predicted with a lower porosity. The importance of low permeability and porosity for improving long-term durability and safety was therefore highlighted.

In the third project year, 2025, the performance of cementitious materials exposed to more complicated scenarios is simulated and investigated solutions, i.e., groundwater and seawater. The results provide us with a better understanding of concrete when exposed to a more aggressive aqueous environment.

2.2.1 Literature review

Concrete durability in groundwater environments is influenced by a combination of chemical, physical, and long-term exposure factors. Groundwater often contains aggressive agents such as sulfates, chlorides, and dissolved carbon dioxide [22], which can react with cement hydrates, leading to expansion, cracking, and loss of structural integrity. Acidic water accelerates calcium leaching [23], reducing alkalinity and promoting steel corrosion [24], while magnesium and sulfate ions destabilise the cement matrix through ettringite formation [1]. Continuous saturation and hydrostatic pressure increase permeability and microcracking risks, especially under thermal cycling in underground structures. A specific example is the durability performance of concrete structures in NPPs and repositories, which are exposed to groundwater conditions. [26] investigates concrete specimens stored for 25 years in environments simulating low and intermediate level waste (LILW) repositories, including groundwater. The findings showed that groundwater can contain chlorides, sulfates, and magnesium, which were potential agents of chemical attack on concrete. However, chloride ingress in groundwater was minimal, with chloride contents well below corrosion thresholds, indicating a low risk of reinforcement corrosion under these conditions. Sulfate and magnesium contents were also low and did not exceed critical limits, and no significant damage or deterioration was observed in petrographic analyses. Minor local cracks and microstructural changes were detected, but these did not compromise overall durability. The study concludes that, for well-designed concrete, groundwater in Finnish LILW repository conditions does not significantly impair long-term durability, though continued monitoring and research are recommended to confirm performance over even longer periods.

Concrete structures face detrimental degradation concerns when exposed to seawater due to their variety of potentially aggressive ions present, such as chloride, sulphate, magnesium, and carbonate ions [27]. A combined chemical attack by the ions present in seawater occurs in marine-exposed structures. The interaction of chlorides and concrete binders focuses on the physical absorption of chlorides to C-S-H [28], chemical binding in hydrate phases to form Friedel's salts ($C_3A{\cdot}CaCl_2{\cdot}10H_2O$) or Kuzel's salts ($C_3A{\cdot}(CaCl_2)_{0.5}{\cdot}(CaSO_4)_{0.5}{\cdot}10H_2O$). However, chlorides can initiate pitting corrosion [29] of the reinforcement when their concentration at the reinforcement reaches a critical level. Concrete plays a role in binding chlorides, which might slow down the chloride ingress and subsequently the initiation of pitting corrosion [30]. This effect, however, largely depends on the type of cement used. The sulfate attack is another concern for concrete when exposed to seawater. Sulfates in seawater form gypsum with the calcium hydroxide present in the pore solution, which further leads to ettringite formation with the presence of aluminate. The supersaturation of ettringite crystals [31] in pore solution and their formation in the pore structure lead to expansion and cracking. Magnesium present in seawater reacts with the concrete binder to form brucite ($Mg(OH)_2$) at a normal pH of concrete, around 12.5 [32]. Due to its dense microstructure and insolubility, the formation of brucite forms an insoluble layer to protect concrete from further degradation.

2.2.2 Assessment tool

The reactive-transport modelling tool HP1, which couples Hydrus-1D with PHREEQC geochemical code, is used to predict the evolution and profile of mineralogical phases and pore water composition in the cementitious system as a function of time. The simplified cement system, geometry, and input data are presented in this subsection.

2.2.2.1 Simplified cement model

The reactive transport model considers the cementitious system in an initially fully saturated state, and the material has been conceptualised as homogeneous porous media. The chemical processes involved are assumed to evolve under thermodynamic equilibrium, including the reactions between each cementitious material. A thermodynamic database, CEMDATA v18 [33] (https://www.empa.ch/cemdata) – PHREEQC version is used to represent the cement system, where a comprehensive selection of cement hydrates on ordinary Portland cement and alkali-activated materials is available. Moreover, the equilibrium constants (i.e., log K values) for each equilibrium reaction under various conditions, standard molar volumes for each mineral, etc., are available in this thermodynamic database. The calcium silica hydrate is considered the ideal solid solution with six end members (CSHQ-JenD, CSHQ-JenH, CSHQ-TobD, CSHQ-TobH, KSiOH, and NaSiOH), following the CSHQ model proposed in [34]. All cementitious materials are considered fully equilibrated as initial conditions in the reactive transport simulations. The cement hydration calculations have been carried out using the Gibbs energy minimisation approach (with the GEM-Selektor software [34]. It is an assumption in these calculations that aggregates are considered chemically inert in the reactive transport model in this work.

Chemical reactions lead to porosity changes in cementitious materials due to the dissolution/ precipitation of phases, which changes the permeability property of the cementitious barrier. Therefore, the iterative calculation of porosity and permeability is considered an important factor, as feedback, when simulating the chemical evolution in a massive concrete structure. In the case of considering the feedback, the porosity is updated in each time step of the chemical calculations by adding the precipitated phases and removing the dissolved ones in volume fractions. The resulting change of porosity is then transferred to the transport equations as feedback, and the corresponding diffusive properties are updated.

2.2.2.2 Simplified geometry

The schematic layout of the system is presented in Figure 4. The total length of the considered cementitious system is 1 m, and it is divided into 100 elements with $\Delta x=0.01$ m. Boundary conditions (BD) are imposed on two sides of the system. The initial composition of the exposed solution, initial phases, and initial composition of pore solution in the mortar will be defined in section 2.2.2.3.

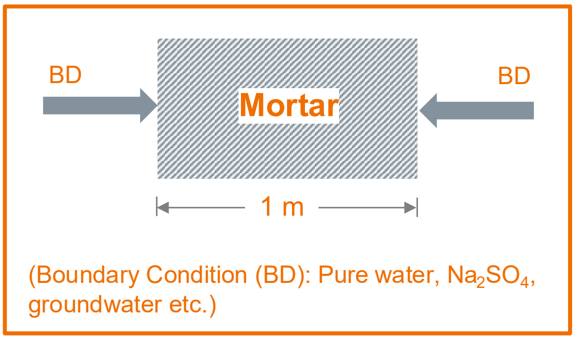

Figure 4: Schematic layout of the simulated cementitious system and the surrounding boundary conditions.

2.2.2.3 Input data

Cementitious materials are assumed to be fully equilibrated under the initial conditions of the reactive transport simulations. The selected mortar material has a high water/binder ratio (1.25) to achieve a highly porous material (porosity of 29%), which accelerates interactions between the material and exposure solutions and consequently degradation phenomena. The mixed design is as follows: 125 g of water, 100 g of CEM I 42.5 N, and 533 g of aggregates. The fully hydrated mortar/concrete includes CH, CSHQ, and calcite as the main minerals, and the C-S-H solid solution shows a relatively higher amount of the JenD (Ca/Si=2.25) and TobD (Ca/Si=1.25) end members. The equilibrated pore water in mortar shows a highly alkaline pH due to the high concentrations of Na+ and K+. The porosity of the mortar (29%) is calculated based on the cement hydration calculations. A bulk diffusion coefficient of 1×10^{-9} m^2/s is selected, which considers the high interconnection of the pore structure in the mortar and a corresponding high impact on transport property. Table 4 summarises the initial mineral phases present in the cementitious materials, and Table 5 shows the composition of the initial pore solution of concrete.

Table 4: Initial mineral phases in cementitious materials (ACED-D2.16).

Mineral [mol/kg water]	Mortar
CSHQ-JenD	1.5092
CSHQ-JenH	0.9835
CSHQ-TobD	1.1345
CSHQ-TobH	0.0486
KSiOH	0.1340
NaSiOH	0.0420
Ettringite	0.1207
Monocarbonate	0.2092
Calcite	0.2445
C3FS0.84H4.32	0.1460
Portlandite	3.6971
Hydrotalcite	0.0822

Table 5: Composition of the pore solution in cementitious materials (ACED-D2.16).

Species [mol/L]	Mortar
pH	13.09
pe	-6.8
Ca	2.65e-3
Mg	2.94e-9
Na	9.13e-3
K	1.53e-1
Fe	4.98e-8
Al	3.30e-5
Cl-	1.95e-7
C(4)	3.33e-5
S(6)	5.54e-4
Si	3.79e-5
Sr	1.00e-10

The mortar interaction with the surrounding environment is simplified to a fixed concentration as a boundary condition, simulating the exposure solutions. In this case, diffusion will be the only process influencing the chemical evolution in the system. Two types of exposure solutions are examined: (i) **Case 1**: groundwater, anticipated degradation of mortar due to leaching and chemical interactions with ions present in groundwater; (ii) **Case 2**: seawater, anticipated leaching and chemical interactions with ions present in seawater. Table 6 summarises the composition of exposure solutions in the two investigation cases.

Table 6: Composition of exposure solutions in cases 1 and 2.

Case 1: Groundwater composition in Olkiluoto in mol/l [35]								
pH	**DIC**	**SO_4**	**Cl**	**Na**	**K**	**Ca**	**Mg**	**Sr**
7.8	4.87e-3	9.58e-4	9.9e-3	1.31e-2	2.48e-4	1.35e-3	7.4e-4	5.71e-6
SIO_2	**Mn**	**Fe**	**S^{2-}**	**F**	**Br**	**NH_4**	**PO_4**	**B**
2.00e-4	3.46e-6	8.06e-6	3.12e-7	3.16e-5	1.75e-5	4.16e-5	1.68e-6	2.68e-5
Case 2: Seawater composition in the Trondheim fjord in mol/l [27].								
Ca	**Mg**	**Na**	**K**	**S**	**Cl**	**C**	-	-
1.08e-2	5.54e-2	4.78e-1	9.7e-3	3.09e-2	6.03e-1	5e-4	-	-

2.2.3 Simulated mineralogical profiles of the cementitious system

2.2.3.1 Simulations of the system in the initial state

Figure 5 shows the initial state of mineralogical phases in the system, where the inert phase, i.e., aggregates, is marked in grey, and the empty space represents porosity in mortar. The initial volume fraction of aggregates is around 56% and the initial porosity is 29%. The pH value is shown on the secondary axis on the right, which has a highly alkaline pH above 13 at the initial state.

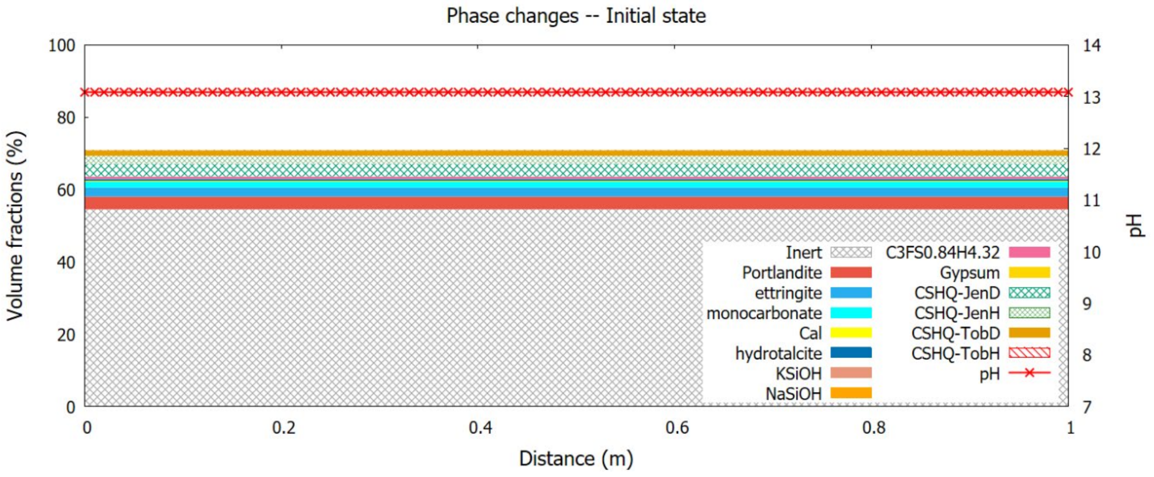

Figure 5: Initial mineralogical phases present in the considered cementitious system.

2.2.3.2 **Case 1**: Simulations of the mortar performance exposed to groundwater

Figure 6 -- Figure 8 present comprehensive profiles of the mineralogical phases that develop within a cementitious matrix up to a century of continuous interaction with groundwater. This long-term exposure initiates a series of chemical and physical transformations, fundamentally altering the composition and durability of the material. The following analyses focus on the profile illustrated in Figure 8.

Dissolution of CH and C-S-H: At a depth of 0.1 meters from the exposed surface, CH is observed to be almost entirely dissolved. This dissolution is a hallmark of aggressive leaching, where groundwater acts as a solvent, extracting calcium ions and thereby destabilising the cement matrix. Alongside CH, C-S-H is also subject to dissolution, albeit at a slower rate and with less intensity. The kinetics of C-S-H dissolution are governed by its slower solubility and more complex structure, which resists rapid breakdown compared to CH. In the degraded zone, particularly where CH and C-S-H have been depleted, there is a tendency for secondary phases such as CSHQ-TobH to form. These phases represent more stable, lower-calcium silicate hydrates, often resembling mineral tobermorite. Their formation is indicative of the system's attempt to re-equilibrate, as the remaining silica and magnesium in the pore solution precipitate into new, less soluble compounds.

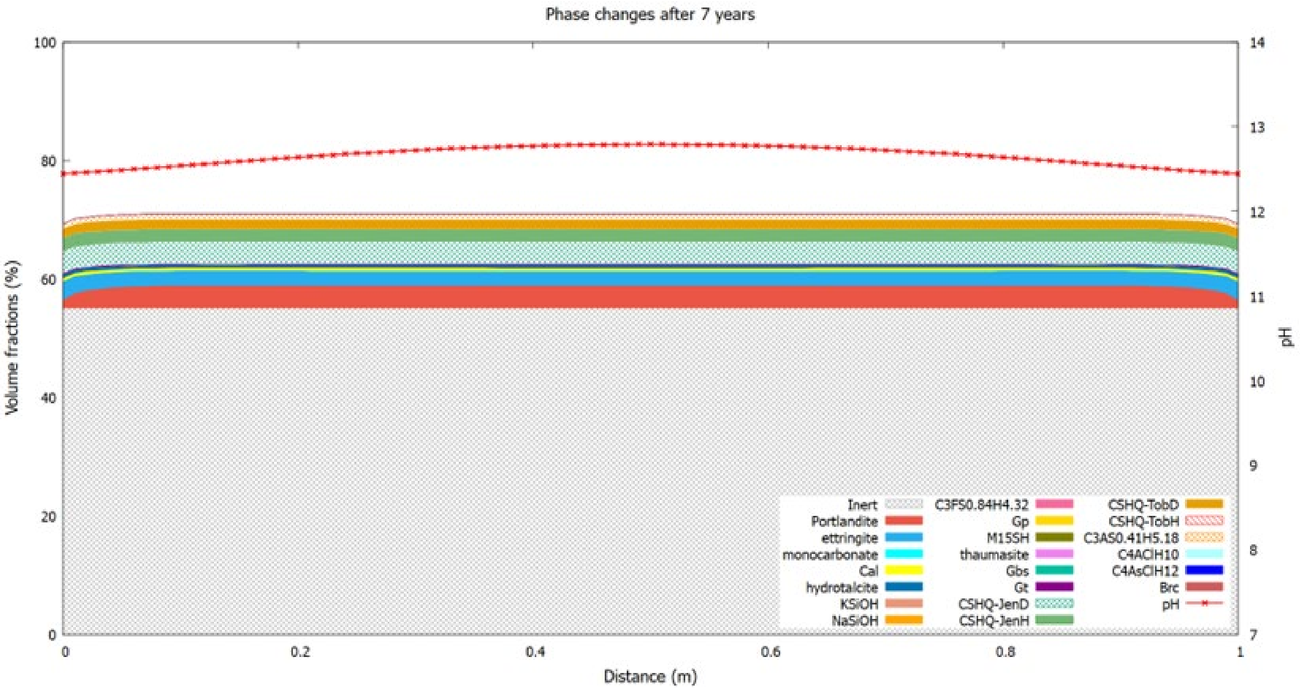

Figure 6: Profile of the mineralogical phases present in the considered cementitious system after being exposed to groundwater for up to 7 years.

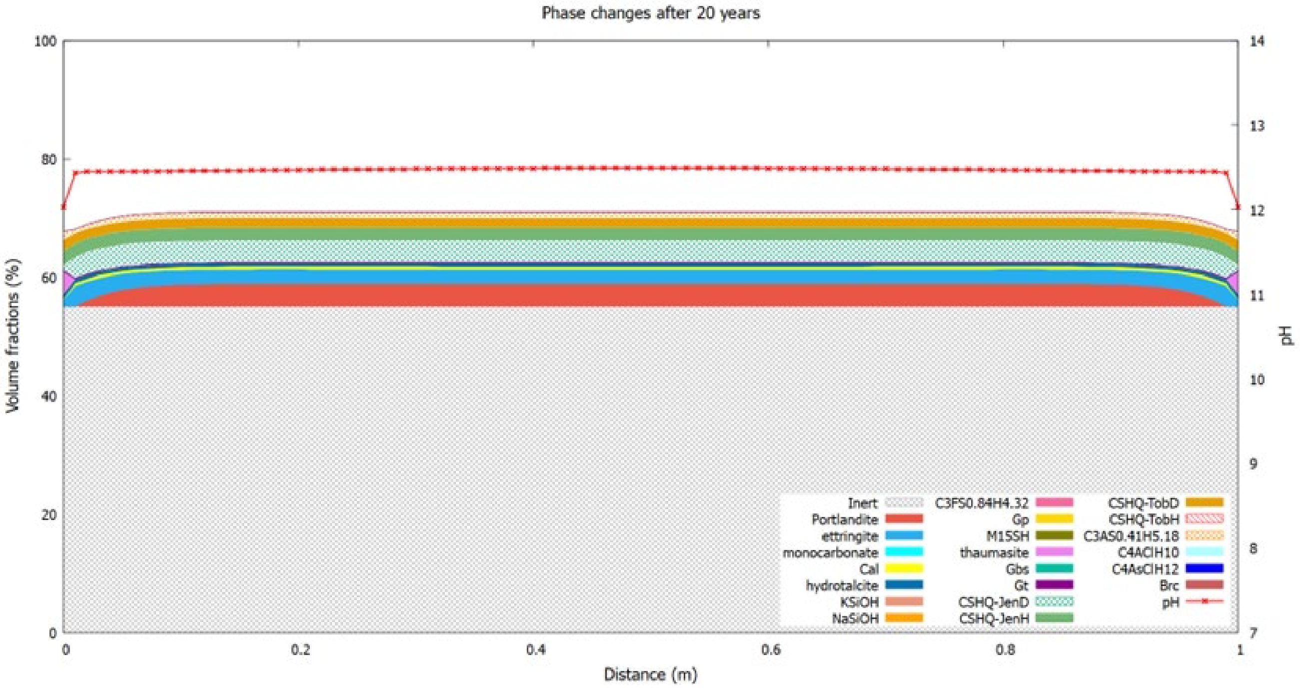

Figure 7: Profile of the mineralogical phases present in the considered cementitious system after being exposed to groundwater for up to 20 years.

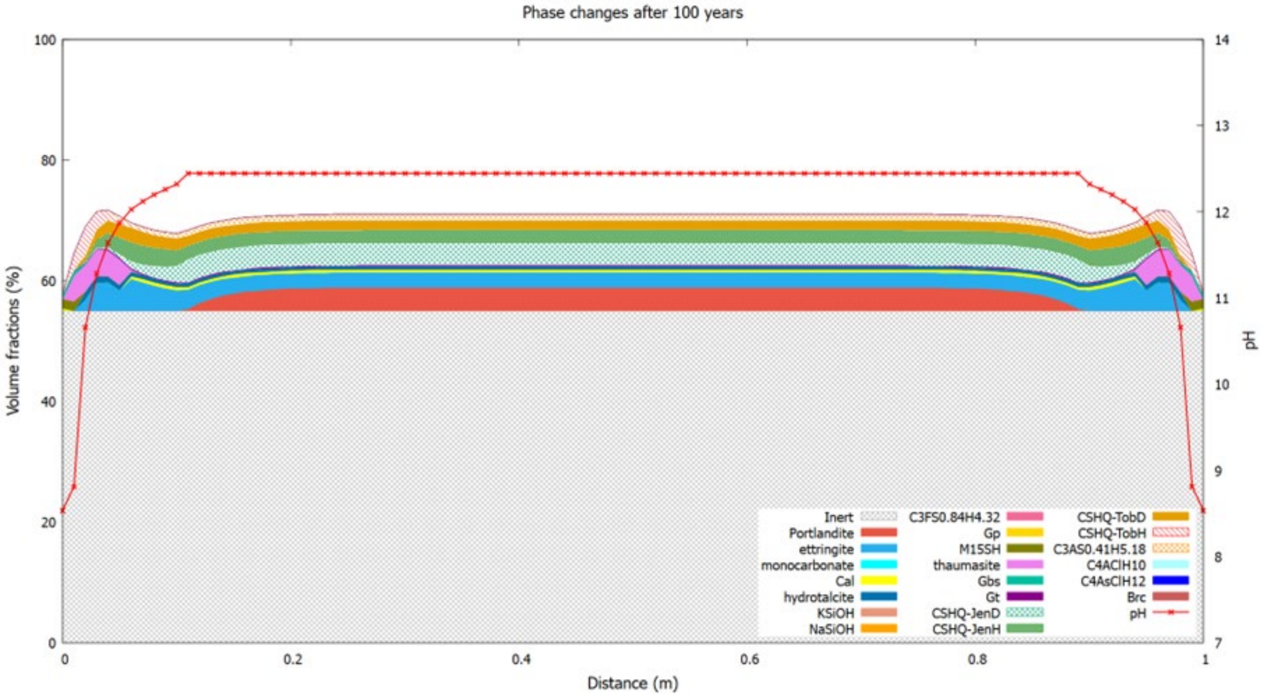

Figure 8: Profile of the mineralogical phases present in the considered cementitious system after being exposed to groundwater for up to 100 years.

Sulfate attack and formation of ettringite and thaumasite: The most significant degradation mechanism observed is sulfate attack. Sulfate ions, present in groundwater, react with the aluminate and calcium phases in cement to form expansive minerals such as ettringite and thaumasite. Ettringite formation leads to internal expansion and cracking, while thaumasite can cause severe softening and loss of structural integrity, especially at low temperatures and in the presence of carbonate ions. These minerals gradually replace the original cement paste, leading to progressive deterioration of the concrete.

Magnesium effects and M-S-H formation: Magnesium ions from groundwater can substitute for calcium in the C-S-H structure, resulting in the formation of magnesium silicate hydrate (M-S-H). This phase is typically confined to the surface region, where magnesium concentrations are highest. The transformation from C-S-H to M-S-H is associated with a reduction in mechanical strength and increased porosity, as M-S-H gels are generally weaker and less cohesive than their calcium counterparts.

Absence of chloride-related precipitation: Despite the presence of chloride ions in groundwater, no significant precipitation of chloride-bearing phases is detected. This is attributed to the relatively low chloride concentration (9.9×10^{-3} mol/l), which is insufficient to drive the formation of phases such as Friedel’s salt or other chloride complexes. As a result, chloride-induced degradation is minimal in this scenario.

pH evolution: The dissolution of CH leads to a marked drop in pH in the affected zone. Initially, cementitious systems maintain a highly alkaline environment (pH close to 13), which is crucial for the stability of hydration products and the passivation of steel reinforcement. However, as CH is leached out, the pH at the surface declines to around 8.5. This reduction in alkalinity not only accelerates the dissolution of other phases but also increases the vulnerability of the system to further chemical attack.

Porosity evolution: Porosity generally increases as CH dissolves and decreases with the formation of secondary phases such as ettringite, thaumasite, CSHQ-TobH, and MSH. However, severe leaching causes a significant rise in ultimate porosity, as nearly all hydrates dissolve. After 100 years of exposure to groundwater, porosity increased from 29% to a maximum of ~43% in the most degraded zone. Changes in porosity influence the transport properties of materials; in other words, higher porosity results in a higher diffusion coefficient, which consequently accelerates the degradation process.

The observed mineralogical transformations in cementitious materials after 100 years of groundwater exposure have profound implications for the durability and design of underground structures. The dissolution of key phases like CH and C-S-H, combined with the formation of expansive minerals such as ettringite and thaumasite due to sulfate attack, highlights the vulnerability of concrete to chemical degradation in aggressive environments. The emergence of M-S-H at the surface further signals a reduction in mechanical strength, while the absence of chloride-related precipitates suggests that low chloride concentrations may mitigate certain risks. These findings underscore the importance of selecting appropriate materials and protective strategies, such as sulfate-resistant cements and supplementary binders, to ensure the long-term stability and safety of infrastructure exposed to groundwater.

2.2.3.3 **Case 2**: Simulations of the mortar performance exposed to seawater

Figure 9 illustrates the distribution of mineralogical phases within the mortar after seven years of exposure to seawater. The simulation was terminated because calcium-bearing phases at the surface had completely dissolved. One contributing factor to the short service life is the poor quality of the material selected, which has a porosity of 29%. Another factor is the high aggressiveness of the seawater environment, which significantly accelerates the overall degradation process.

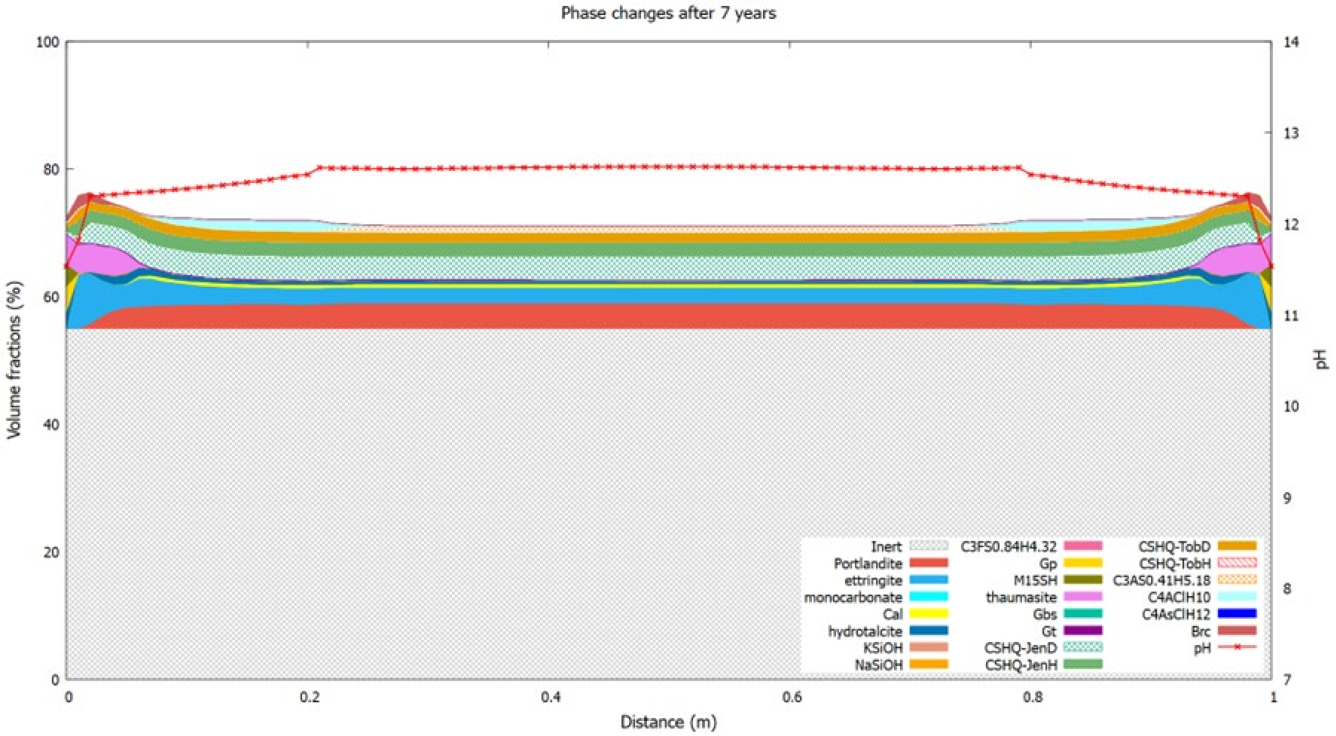

Figure 9: Profile of the mineralogical phases present in the considered cementitious system after being exposed to seawater for 7 years.

Dissolution of CH and C-S-H: After prolonged exposure, the dissolution of CH remains minimal beyond a depth of 0.02 m. This change is partly due to leaching, where seawater acts as a solvent, extracting calcium ions and destabilising the cement matrix. Alongside CH, C-S-H also undergoes dissolution, though at a slower rate and with less intensity. At the same time, calcium released from CH and C-S-H contributes to the formation of new phases such as thaumasite, ettringite, and Friedel's salts. This pattern indicates that chemical interaction with seawater is more complex than simple leaching: rather than calcium ions being lost to the surrounding solution, they actively participate in forming new compounds.

Sulfate attack and formation of ettringite and thaumasite: Within the degraded depth of 0.1m, a substantial amount of ettringite and thaumasite is observed to have precipitated. Sulfate ions present in seawater react with the aluminate and calcium phases in the cement matrix, forming expansive minerals such as ettringite and thaumasite. These minerals progressively replace the original cement paste, leading to continuous deterioration of the concrete.

Magnesium effects and M-S-H formation: Magnesium ions present in seawater can replace calcium within the C-S-H structure, leading to the formation of M-S-H. In addition to M-S-H, brucite is commonly observed as a secondary phase. The precipitation of brucite further impacts the pore structure and may contribute to localised expansion, although its protective effect against chloride ingress is limited. Overall, the presence of magnesium accelerates the decalcification process and promotes long-term deterioration of concrete exposed to marine environments.

Chloride-related precipitation: Chloride ions from seawater penetrate deeply into the concrete matrix, leading to the extensive formation of Friedel's salts up to 0.3 m from the surface. These chloride-bearing compounds form through reactions between chloride ions and aluminates in the cement paste. While Friedel's salts can temporarily immobilize chlorides, their formation significantly replaces phases such as CSHQ-TobH, reducing the structural integrity of the matrix. Over time, this substitution weakens the cementitious network and increases vulnerability to further chemical attacks, particularly when chloride binding capacity is exceeded. This mechanism plays a critical role in the overall degradation process under aggressive marine conditions.

pH evolution: The pH shows a slight decrease, from approximately 12.5 to about 11.5. This limited drop can be attributed to the minor dissolution of CH, which acts as a pH buffer in cementitious materials. As leaching progresses, the pH value will continue to decline accordingly.

Porosity evolution: As noted earlier, porosity generally increases with the dissolution of CH and decreases with the formation of secondary phases such as ettringite, thaumasite, CSHQ-TobH, and M-S-H. In this case, due to the limited leaching observed, porosity does not change significantly. Instead, the formation of new phases tends to reduce porosity in the degraded zone—from 29% to a minimum of approximately 23%. This reduction in porosity is beneficial for the material's service life, as it slows down transport processes and, consequently, the rate of degradation.

Similar to Case 1, sulfate attack is evident, leading to the precipitation of ettringite and thaumasite in the degraded zone. Additionally, magnesium ions replace calcium in the C-S-H structure near the surface, resulting in the formation of M-S-H. A key difference from Case 1 is the widespread precipitation of Friedel's salts between 0.1 and 0.3 m from the surface, driven by the relatively high chloride concentration in seawater (6.03×10^{-1} mol/l). Brucite formation is also observed at approximately 0.1 m depth.

Compared to mortar exposed to groundwater, the degradation under seawater conditions is markedly more severe, reflecting the aggressive chemical environment. However, it is important to note that the current reactive transport model does not account for chloride adsorption within C-S-H, meaning that interactions between chloride and this phase were excluded. If chloride adsorption within C-S-H were considered, a smaller amount of chloride would remain available for chemical reactions, resulting in fewer associated phase changes. Furthermore, the current model omits kinetic constraints, effectively simulating an accelerated degradation process rather than real-time progression. A more advanced model incorporating kinetic effects would provide a more realistic scenario with slower degradation rates, which is possible using the iCP simulation platform.

2.2.4 Subconclusion

To sum up, the primary degradation phenomena observed when mortar is exposed to groundwater and seawater include:

- Calcium leaching, which occurs in CH and C-S-H phases;
- Chloride binding, where chlorides react with calcium aluminate hydrates to form Friedel's salts;
- Sulfate attack, in which sulfates react with calcium hydroxide to form gypsum, which subsequently reacts with aluminates to produce ettringite. Additionally, thaumasite may form, particularly at a temperature below 15°C.
- Magnesium-related effects, where magnesium replaces calcium in C-S-H, leading to the formation of M-S-H. Furthermore, brucite precipitation occurs at the typical concrete pH (around 12.5), creating an insoluble layer that may offer some protection.

The severity of each degradation mechanism is influenced by the aggressiveness of the exposure conditions with respect to the relevant chemical elements. Based on the findings of this study, calcium leaching emerges as the most critical mechanism due to its extensive nature and the essential role of CH and C-S-H in maintaining the mechanical performance of mortar. Sulfate attack ranks second, as it is highly pervasive and the expansive nature of the precipitated crystals can cause significant damage to the cementitious matrix. Chloride binding also warrants attention when sufficient chloride is present, such as in seawater, since the formation of Friedel's salts can displace phases like CSHQ-Tob, thereby compromising the structural integrity of the matrix. In contrast, magnesium-related effects are considered limited because of the low magnesium concentration in the exposure solutions; moreover, the precipitation of brucite may even offer some protection by forming an insoluble layer.

To mitigate mortar deterioration from seawater and groundwater exposure, use sulfate-resistant or blended cements with supplementary materials like slag or silica fume to reduce permeability and chemical attack, maintain a low water-to-cement binder ratio for densification, and apply waterproofing admixtures or polymer modifiers for added protection. Surface coatings such as geopolymer or cement-based layers can further block chloride ingress while increasing concrete cover, and considering corrosion-resistant reinforcement helps safeguard structural integrity. Complement these measures with proper drainage design, sealants for joints, and regular monitoring using durability models to detect early signs of cracking or leaching, ensuring long-term performance in aggressive environments.

3. Conclusions and summary

This report summarises the work that has been done in WP2 of the SAFER-FN-CAMP project during 2025.

In the **first** task, the reviewed studies highlight that ASR-induced volumetric strain is strongly influenced by the stress state and degree of confinement. While some early works suggested constant volumetric strain regardless of stress, more recent investigations confirm that confinement significantly mitigates ASR expansion and redistributes strain toward less restrained directions. This redistribution often results in anisotropic damage development, affecting stress distribution, crack patterns, and long-term structural integrity. To capture this behaviour, a systematic method for calculating weight factors was introduced, enabling proportional distribution of volumetric ASR strain among the three principal directions under varying loading conditions. This approach involves identifying the stress quadrant based on compressive and tensile limits, determining node weights through interpolation, computing shape factors to quantify node influence, and aggregating these contributions to derive final weight factors. By reflecting the relative confinement imposed by applied stresses, this method provides a framework for modelling strain redistribution under uniaxial, biaxial, and triaxial loading. Validation against experimental data demonstrates good agreement for some studies, confirming its reliability for engineering applications. However, discrepancies observed in complex stress states underscore the limitations of simplified assumptions and the need for advanced predictive models.

Future work, as proposed in FN-CAMP II, will extend this methodology into a **multi-scale modelling framework** that integrates chemical kinetics, microstructural evolution, and time-dependent phenomena such as creep and shrinkage. This will enable accurate simulation of ASR and related internal swelling reactions, supporting improved assessment and mitigation strategies for critical infrastructure, including nuclear power plant structures.

In the **second** task, the performance of mortars exposed to groundwater and seawater was investigated. Mortar durability in groundwater and seawater environments is governed by complex chemical and physical interactions that evolve over long exposure periods. Groundwater typically contains sulfates, chlorides, and magnesium, which can induce leaching of calcium hydroxide (CH) and destabilise calcium silicate hydrates (C-S-H), while promoting secondary phase formation such as ettringite and magnesium silicate hydrates (M-S-H).

However, studies on Finnish low- and intermediate-level waste (LILW) repository conditions indicate that chloride, sulfate, and magnesium concentrations remain below critical thresholds, resulting in minimal deterioration over 25 years. Petrographic analyses revealed only minor microstructural changes, confirming that well-designed concrete can maintain durability under these groundwater conditions, though continued monitoring is essential for extended service life.

In contrast, seawater exposure presents a significantly more aggressive environment due to its high chloride and sulfate content. Chlorides penetrate concrete and react with aluminates to form Friedel’s salts, while sulfates induce gypsum and ettringite formation, leading to expansion and cracking. Magnesium ions further degrade C-S-H by forming M-S-H, and brucite precipitation occurs near the surface. Reactive transport simulations confirm accelerated dissolution of CH and C-S-H phases, widespread Friedel’s salt formation, and notable pH reduction, all of which compromise structural integrity. Compared to groundwater, seawater-induced degradation is more severe and rapid, underscoring the need for targeted mitigation strategies.

To address these challenges, durability design should incorporate sulfate-resistant or blended cements with supplementary materials (e.g., slag, silica fume) to reduce permeability and chemical attack.

Additional measures include maintaining a low water-to-cement ratio, applying waterproofing admixtures, and using surface coatings to block chloride ingress. Increasing concrete cover, employing corrosion-resistant reinforcement, and implementing drainage systems further enhance protection. Finally, predictive tools such as reactive transport models (e.g., HP1 coupled with PHREEQC) should be integrated into long-term monitoring programs to anticipate chemical evolution and detect early signs of deterioration. These combined strategies are essential for ensuring the long-term performance and safety of concrete structures in aggressive groundwater and marine environments.

4. References

[1] Y. Gu, “Assessment of alkali-silica reaction and aggressive aqueous attack in concrete 2023,” 2023, VTT internal report, VTT-R-00023-24.

[2] Y. Gu, “SAFER-FN-CAMP: Assessment of alkali-silica reaction and aggressive aqueous attack in concrete 2024,” 2024, VTT internal report, VTT-R-00725-24.

[3] V. Saouma; L. Perotti, “Constitutive Model for Alkali-Aggregate Reactions,” *ACI Mater J*, vol. 103, no. 3, p. 194, 2006, doi: 10.14359/15853.

[4] S. Multon and F. Toutlemonde, “Effect of applied stresses on alkali–silica reaction-induced expansions,” *Cem Concr Res*, vol. 36, no. 5, pp. 912–920, May 2006, doi: 10.1016/j.cemconres.2005.11.012.

[5] B. P. Gautam and D. K. Panesar, “A new method of applying long-term multiaxial stresses in concrete specimens undergoing ASR, and their triaxial expansions,” *Mater Struct*, vol. 49, no. 9, pp. 3495–3508, Sep. 2016, doi: 10.1617/s11527-015-0734-z.

[6] P. Morenon, S. Multon, A. Sellier, E. Grimal, F. Hamon, and E. Bourdarot, “Impact of stresses and restraints on ASR expansion,” *Constr Build Mater*, vol. 140, pp. 58–74, Jun. 2017, doi: 10.1016/j.conbuildmat.2017.02.067.

[7] A. E. K. Jones and L. A. Clark, “The effects of restraint on ASR expansion of reinforced concrete,” *Magazine of Concrete Research*, vol. 48, no. 174, pp. 1–13, Mar. 1996, doi: 10.1680/macr.1996.48.174.1.

[8] T. M. A. Ahmed, E. Burley, and S. R. Rigden, “The effect of alkali—silica reaction on the fatigue behaviour of plain concrete tested in compression, indirect tension and flexure,” *Magazine of Concrete Research*, vol. 51, no. 6, pp. 375–390, Dec. 1999, doi: 10.1680/macr.1999.51.6.375.

[9] C. F. Dunant and K. L. Scrivener, “Effects of uniaxial stress on alkali–silica reaction induced expansion of concrete,” *Cem Concr Res*, vol. 42, no. 3, pp. 567–576, Mar. 2012, doi: 10.1016/j.cemconres.2011.12.004.

[10] S. Multon, J-F. Seignol;, and Fo Toutlemonde;, “Structural behavior of concrete beams affected by alkali-silica reaction,” *ACI Mater J*, vol. 102, no. 2, p. 67, 2005.

[11] H. Kagimoto, Y. Yasuda, and M. Kawamura, “ASR expansion, expansive pressure and cracking in concrete prisms under various degrees of restraint,” *Cem Concr Res*, vol. 59, pp. 1–15, May 2014, doi: 10.1016/j.cemconres.2014.01.018.

[12] M. Berra, G. Faggiani, T. Mangialardi, and A. E. Paolini, “Influence of stress restraint on the expansive behaviour of concrete affected by alkali-silica reaction,” *Cem Concr Res*, vol. 40, no. 9, pp. 1403–1409, Sep. 2010, doi: 10.1016/j.cemconres.2010.05.002.

[13] D. M. Wald, M. T. Allford, O. Bayrak, and T. D. Hrynyk, “Development and multiaxial distribution of expansions in reinforced concrete elements affected by alkali–silica reaction,” *Structural Concrete*, vol. 18, no. 6, pp. 914–928, Dec. 2017, doi: 10.1002/suco.201600220.

[14] D. Wald, G. A. Martinez, and O. Bayrak, “Expansion behavior of a biaxially reinforced concrete member affected by alkali-silica reaction,” *Structural Concrete*, vol. 18, no. 4, pp. 550–560, Aug. 2017, doi: 10.1002/suco.201600143.

[15] S. S. Kongshaug, O. Oseland, T. Kanstad, M. A. N. Hendriks, E. Rodum, and G. Markeset, “Experimental investigation of ASR-affected concrete – The influence of uniaxial loading on the evolution of mechanical properties, expansion and damage indices,” *Constr Build Mater*, vol. 245, p. 118384, Jun. 2020, doi: 10.1016/j.conbuildmat.2020.118384.

[16] A. Allard, S. Bilodeau, F. Pissot, B. Fournier, J. Bastien, and B. Bissonnette, “Expansive behavior of thick concrete slabs affected by alkali-silica reaction (ASR),” *Constr Build Mater*, vol. 171, pp. 421–436, May 2018, doi: 10.1016/j.conbuildmat.2018.03.159.

[17] L. J. STRUBLE and S. DIAMOND, “Swelling Properties of Synthetic Alkali Silica Gels,” *Journal of the American Ceramic Society*, vol. 64, no. 11, pp. 652–655, Nov. 1981, doi: 10.1111/j.1151-2916.1981.tb15864.x.

[18] C. Larive, “Apports combinés de l’expérimentation et de la modélisation à la compréhension de l’alcali-réaction et de ses effets mécaniques,” Ecole nationale des ponts et chaussees, 1997.

[19] J. Liaudat, I. Carol, C. M. López, and V. E. Saouma, "ASR expansions in concrete under triaxial confinement," *Cem Concr Compos*, vol. 86, pp. 160–170, Feb. 2018, doi: 10.1016/j.cemconcomp.2017.10.010.

[20] B. P. et al. Gautam, "Multiaxial Expansion-Stress Relationship for Alkali Silica Reaction-Affected Concrete," *ACI Mater J*, vol. 114, no. 1, 2017.

[21] S. Multon, "Evaluation expérimentale et théorique des effets mécaniques de l'alcali-réaction sur des structures modèles," Université de Marne-la-Vallée, 2003.

[22] D. Nelson, *Natural variations in the composition of groundwater*. Drinking Water Program, Oregon Department of Human Services, 2002.

[23] B. Gérard, C. Le Bellego, and O. Bernard, "Simplified modelling of calcium leaching of concrete in various environments," *Mater Struct*, vol. 35, no. 10, pp. 632–640, Dec. 2002, doi: 10.1007/BF02480356.

[24] B. Y. Fang, A. Atrens, J. Q. Wang, E. H. Han, Z. Y. Zhu, and W. Ke, "Review of stress corrosion cracking of pipeline steels in 'low' and 'high' pH solutions," *J Mater Sci*, vol. 38, no. 1, pp. 127–132, Jan. 2003, doi: 10.1023/A:1021126202539.

[25] A. Ba Ragaa, "Long-term durability testing of concrete in low and intermediate level waste repositories.," 2023.

[26] K. De Weerdt, H. Justnes, and M. R. Geiker, "Changes in the phase assemblage of concrete exposed to sea water," *Cem Concr Compos*, vol. 47, pp. 53–63, Mar. 2014, doi: 10.1016/j.cemconcomp.2013.09.015.

[27] Y. Zhang *et al.*, "Chloride absorption capacity of calcium silicate hydrate (C-S-H) and its effect on steel corrosion in simulated concrete pore solution," *J Sustain Cem Based Mater*, vol. 12, no. 12, pp. 1548–1563, Dec. 2023, doi: 10.1080/21650373.2023.2243477.

[28] K. V. Akpanyung and R. T. Loto, "Pitting corrosion evaluation: a review," *J Phys Conf Ser*, vol. 1378, no. 2, p. 022088, Dec. 2019, doi: 10.1088/1742-6596/1378/2/022088.

[29] A. Goyal, H. S. Pouya, E. Ganjian, and P. Claisse, "A Review of Corrosion and Protection of Steel in Concrete," *Arab J Sci Eng*, vol. 43, no. 10, pp. 5035–5055, Oct. 2018, doi: 10.1007/s13369-018-3303-2.

[30] Y. Gu, P. Dangla, R. P. Martin, O. Omikrine Metalssi, and T. Fen-Chong, "Modeling the sulfate attack induced expansion of cementitious materials based on interface-controlled crystal growth mechanisms," *Cem Concr Res*, vol. 152, 2022, doi: 10.1016/j.cemconres.2021.106676.

[31] N. R. Buenfeld and J. B. Newman, "The development and stability of surface layers on concrete exposed to sea-water," *Cem Concr Res*, vol. 16, no. 5, pp. 721–732, Sep. 1986, doi: 10.1016/0008-8846(86)90046-3.

[32] B. Lothenbach *et al.*, "Cemdata18: A chemical thermodynamic database for hydrated Portland cements and alkali-activated materials," *Cem Concr Res*, vol. 115, 2019, doi: 10.1016/j.cemconres.2018.04.018.

[33] D. A. Kulik, "Improving the structural consistency of C-S-H solid solution thermodynamic models," *Cem Concr Res*, vol. 41, no. 5, pp. 477–495, May 2011, doi: 10.1016/j.cemconres.2011.01.012.

[34] P. Hellä, P. Pitkänen, J. Löfman, S. Partamies, U. Vuorinen, and P. Wersin, *Safety case for the disposal of spent nuclear fuel at Olkiluoto. Definition of reference and bounding groundwaters buffer and backfill porewaters*. Posiva Oy, 2014.